Correlation of the Orthogonal Basis of the Core Plasma Distribution to the Divertor Footprint Distribution in LHD*)

Hirohiko TANAKA, Suguru MASUZAKI[1,2)], Gakushi KAWAMURA[1,2)], Yuki HAYASHI[1,2)], Masahiro KOBAYASHI[1,2)], Yasuhiro SUZUKI[3)], Kiyofumi MUKAI[1,2)], Shin KAJITA[4)] and Noriyasu OHNO

Nagoya University, Nagoya 464-8603, Japan
[1)]*National Institute for Fusion Science, National Institutes of Natural Sciences, Toki 509-5292, Japan*
[2)]*The Graduate University for Advanced Studies, SOKENDAI, Toki 509-5292, Japan*
[3)]*Hiroshima University, Hiroshima 739-8527, Japan*
[4)]*The University of Tokyo, Chiba 277-8561, Japan*

(Received 1 December 2022 / Accepted 27 February 2023)

We have applied the multivariable analysis technique called the proper orthogonal decomposition (POD) to both the divertor particle flux distribution and the electron pressure distribution in the core region of LHD. The cross-correlation analysis indicates that 3rd, 4th, and 5th POD modes of the electron pressure distribution are highly correlated with the divertor footprint index which is a measure of where the peak position of the particle flux distribution is located on the inner divertor plate. Both the 3rd and 4th modes seem to correspond to the shift of the electron pressure peak position from the magnetic-axis radius. In contrast, 5th mode has a strong influence on the peripheral gradient of the electron pressure distribution. Their relationships with the divertor footprint could be explained by the finite β and the Pfirsch-Schlüter current effects.

Keywords: proper orthogonal decomposition, divertor footprint, toroidal divertor probe array, Thomson scattering, LHD

DOI: 10.1585/pfr.18.2402021

1. Introduction

It is essential to keep the divertor heat load below the material tolerance for a successful fusion reactor, and an accurate understanding of the formation mechanism of the divertor footprint distribution is indispensable for the heat load estimation. On the low-field side divertor plate in the tokamak configuration, the heat flux distribution can be fitted by convolving an exponential decay and a Gaussian function, and fitting parameters in several devices were collected in a database [1]. In contrast, such a simple model cannot be used in the heliotron/stellarator configuration; for example, the footprint distribution has multiple peaks across the strike point. Because of the complicated three-dimensional (3D) magnetic field geometry and the presence of a stochastic region, understanding the relationship between the magnetic field structure and the divertor footprint is difficult and is continuously progressing [2–4].

In the Large Helical Device (LHD), the divertor heat and particle flux distributions are thought to be mainly determined by the magnetic configuration, which depends on the external control parameters such as the magnetic axis position R_{ax}, cancellation rate of the quadrupole magnetic field component B_{q}, and the coil pitch parameter γ. In addition, the plasma current against the toroidal magnetic field strength ($I_{\mathrm{p}}/B_{\mathrm{t}}$) [5] and high plasma pressure with high averaged beta ($\langle\beta\rangle$) [6] could modify the magnetic geometry. Furthermore, it was suggested that edge electron temperature affects the peaking position of the footprint profile [7], which was not reproduced by the EMC3-EIRENE simulation even if the spatially non-uniform transport coefficients were introduced [8].

In recent studies, we have applied the proper orthogonal decomposition (POD) method, which is also called the principal component analysis (PCA) and one of the multivariable analysis techniques, to the ion-saturation-current dataset obtained by using a large number of Langmuir probes embedded on the LHD divertor plates (called "toroidal divertor probe arrays") [9,10]. As a result, a characterization index of the divertor particle flux distribution ($r_{2/1}$) was evaluated from the ratio of two dominant orthogonal bases in the POD analysis outputs. Moreover, the obtained $r_{2/1}$ was found to be correlated with the peripheral electron pressure gradient even if $\langle\beta\rangle$ is not so high [9]. This suggests that the plasma pressure distribution alters the edge magnetic field structure, which in turn changes the divertor footprint distribution.

In this study, to promote the further understanding of the relationship between the core plasma and the divertor footprint distributions, we have applied the POD method

author's e-mail: h-tanaka@ees.nagoya-u.ac.jp
*) This article is based on the presentation at the 31st International Toki Conference on Plasma and Fusion Research (ITC31).

to the Thomson scattering (TS)-measured upstream electron pressure distribution in addition to the divertor probe signals. Dominant orthogonal bases of the electron pressure were found and their correlations with the above-mentioned $r_{2/1}$ were calculated. As a result, we confirmed relationships being consistent with previous studies.

Section 2 describes the dataset creation, which is an important preliminary step in multivariable analysis. Section 3 explains POD method and the divertor footprint characterization index obtained in the previous study [9]. The POD analysis results of core plasma distribution and their relationships with the divertor footprint are shown in section 4. Finally, this study is summarized in section 5.

2. Creating Datasets

In this study, we applied the POD method to two datasets, dataset A and dataset B, obtained in the 17th experimental campaign in LHD. Dataset A is the same with the previous study in Ref. [9], which was used to characterize the divertor particle flux distribution. Dataset B is a part of dataset A with fewer time points for analyzing the TS-measured upstream electron pressure, as described later. All data was downloaded from the Kaiseki Data Server System [11].

Dataset A contains various measured data, including ion saturation current signals measured with probe arrays across the strike point on 10 divertor plates (named 2L, 2R, 6L, 6R, 7L, 7R, 8L, 8R, 10L, and 10R) and TS-measured parameters, in discharges with a standard inward-shifted magnetic configuration ($R_{\mathrm{ax}} = 3.6\,\mathrm{m}$, $B_{\mathrm{q}} = 100\%$, and $\gamma = 1.254$) with strong toroidal magnetic field strength ($B_{\mathrm{t}} = -2.75\,\mathrm{T}$). The discharge gas was basically hydrogen, and no distinction was made for the inclusion of impurity gases. Data were extracted in 0.1 s increments from a discharge time from 3 to 7 s. Furthermore, to remove the plasma-current effect, time points satisfying $|I_{\mathrm{p}}/B_{\mathrm{t}}| < 10\,\mathrm{kA/T}$ condition was selected. In addition, time points with upstream plasma and no measurement problems were extracted. As a result, an ion saturation current matrix ($I(x, s)$) was created for 6409 time points (s) in 276 discharges at a total of 188 probe-channel positions (x), excluding frequently damaged channels (see Fig. 2 in Ref. [9]).

Time points in dataset B were extracted under more stringent condition than in dataset A. Regarding upstream electron temperature T_{e} and electron density n_{e}, time points containing one or more TS channels with a large error ratio with $\Delta T_{\mathrm{e}}/T_{\mathrm{e}} > 50\%$ or $\Delta n_{\mathrm{e}}/n_{\mathrm{e}} > 50\%$ were excluded. Here, TS channels where errors were often large were initially excluded. This data extraction process excludes noise-induced spatial structure in the POD analysis result. As a result, the electron pressure $p_{\mathrm{e}}(R, t) = n_{\mathrm{e}}T_{\mathrm{e}}$ for 1089 time points (t) in 118 discharges at 110 radial positions (R) are obtained, as shown in Fig. 1.

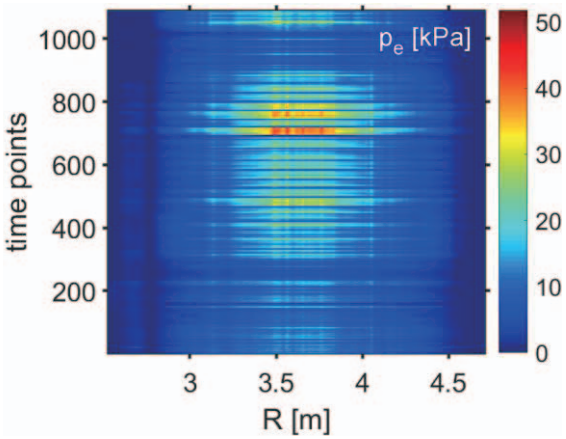

Fig. 1 2D pattern of p_{e} as functions of the major radius R and the time point t.

3. POD Analysis Procedure

2D matrixes of the ion saturation current I in database A and the electron pressure p_{e} in database B were analyzed by the POD method, which does not use any artificial orthogonal function [12,13] and is generally the same or similar to other multivariable analysis methods, e.g., PCA and singular value decomposition (SVD). Such the multivariable methods have been often applied to magnetic confinement plasmas [14–16]. In this study, the POD analysis procedure of the matrix I is the same as the previous study [9].

First, a fluctuation component of the matrix $I(x, s)$ as functions of position x and time point s was calculated as $\tilde{I}(x, s) = I - \langle I \rangle$, where $\langle\ \rangle$ means the average in time point. Next, the covariance matrix $\mathbf{C}$ was calculated from the cross-correlation function C_{lm} between positions x_l and x_m as

$$\mathbf{C} = \begin{pmatrix} C_{11} & \cdots & C_{1n} \\ \vdots & \ddots & \vdots \\ C_{n1} & \cdots & C_{nn} \end{pmatrix}, \tag{1}$$

$$C_{lm} = \langle \tilde{I}(x_l, s)\tilde{I}(x_m, s) \rangle. \tag{2}$$

After that, the eigenfunction $\phi_i(x)$ and the eigenvalue λ_i were calculated from the eigenvalue problem as

$$\mathbf{C}\phi_i(x) = \lambda_i \phi_i(x). \tag{3}$$

The calculated $\phi_i(x)$ is the orthonormal basis for the probe position x. The orthogonal basis for the time point s was then obtained as

$$a_i(s) = \sum_{k=1}^{n} \tilde{I}(x_k, s)\phi_i(x_k). \tag{4}$$

By using $\phi_i(x)$ and $a_i(s)$, $\tilde{I}(x, s)$ can be reconstructed as

$$\tilde{I}(x, s) = \sum_{i=1}^{n} a_i(s)\phi_i(x). \tag{5}$$

In addition, due to the relation of $\langle a_i^2(s) \rangle = \lambda_i$, $\lambda_i / \sum_{k=1}^{n} \lambda_k$ gives the contribution ratio from $a_i(s)\phi_i(x)$ for the variance over the entire space. The subscript i, called a POD mode

number, is descending order of magnitude of λ_i as $\lambda_1 > \lambda_2 > \cdots > \lambda_n$.

Furthermore, the offset-added $a_i(s)$ was also defined as

$$a_i'(s) \equiv a_i(s) + \sum_{k=1}^{n} \langle I(x_k, s) \rangle \phi_i(x_k), \tag{6}$$

which can satisfy

$$I(x, s) = \sum_{i=1}^{n} a_i'(s)\phi_i(x). \tag{7}$$

As reported in the previous study [9], a 2D matrix of the ion saturation current was found to consist predominantly of $i = 1$ and $i = 2$ modes (~87%), so that $I(x, s) \sim a_1'(s)\phi_1(x) + a_2'(s)\phi_2(x)$. Furthermore, it is known that the ratio of a_2' to a_1', $r_{2/1} \equiv a_2'/a_1'$, characterizes the shape of the ion saturation current distribution. Hereafter, we refer to $r_{2/1}$ as the divertor footprint index.

Figure 2 shows examples of reconstructed ion saturation current distributions using different $r_{2/1}$ on 8L and 8R plates, which are positioned in the same toroidal section (#8) with helical symmetry. Here, $\phi_i(x)$ and $a_i(s)$ were calculated from I in dataset A. When $r_{2/1}$ is negative, the divertor particle flux has a sharp peak at the private side with the smaller probe number. In contrast, with a positive $r_{2/1}$, the amplitude of the divertor particle flux becomes larger at the SOL side with the larger probe number. On other divertor plates (2L, 2R, 6L, 6R, 7L, 7R, 10L, and 10R), which were simultaneously analyzed, similar tendencies were found (no figure). The larger amplitude on 8L plate than on 8R plate is attributed to drift transports [6]. Because Fig. 2 consists of the dominant bases from the entire dataset, it should reflect the distribution in the attached divertor state more strongly than the detached state with a limited number of detached plasma discharges.

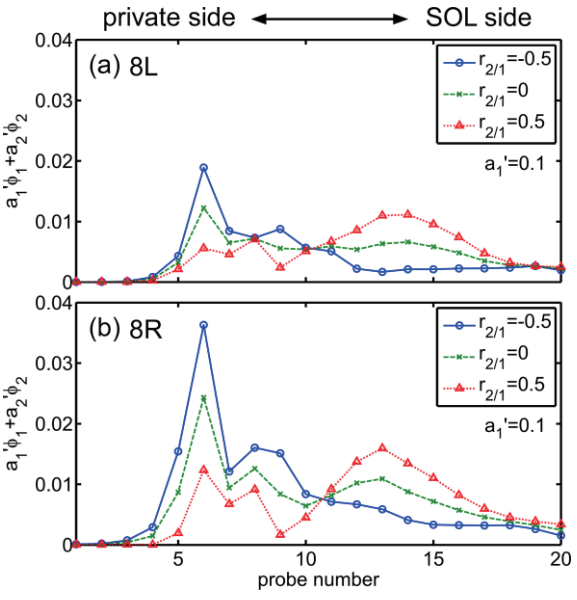

Fig. 2 Reconstructed ion saturation current distributions on (a) 8L and (b) 8R plates with $r_{2/1} = -0.5$ (blue solid line), 0 (green dashed line), and 0.5 (red dotted line).

The same analysis as above is possible for the 2D matrix of the core electron pressure in Fig. 1 as

$$\tilde{p}_e(R, t) = \sum_{i=1}^{N} b_i(t)\psi_i(R), \tag{8}$$

where $\psi_i(R)$ is the orthonormal basis for the radial position R and $b_i(t)$ is the orthogonal basis for the time point t. The contribution ratio from each POD mode can be also calculated with the eigenvalue.

4. Analysis Results

4.1 POD modes of electron pressure distribution

Figure 3 shows ψ_i and its contribution ratio calculated from the electron pressure distribution in dataset B. The $i = 1$ mode has a single peak around the magnetic axis position at $R_{ax} = 3.6$ m and contains ~96% of the variance. Thus, this mode can reconstruct most of the variation in electron pressure distribution. In other words, $i \geq 2$ modes finely modify the electron pressure distribution, e.g., ~2% for $i = 2$ mode and < 1% for $i > 2$ modes.

The shape of ψ_2 has a peak at $R \sim R_{ax}$ and concavity on both inner and outer sides. Therefore, positive/negative b_2 contributes to make the p_e distribution peaking/flattening. Detailed characteristics of ψ_3, ψ_4, and ψ_5 will be discussed later. In the higher order modes, there are finer structures due to measurement noise and so on. In this study, modes with $i > 10$ are ignored.

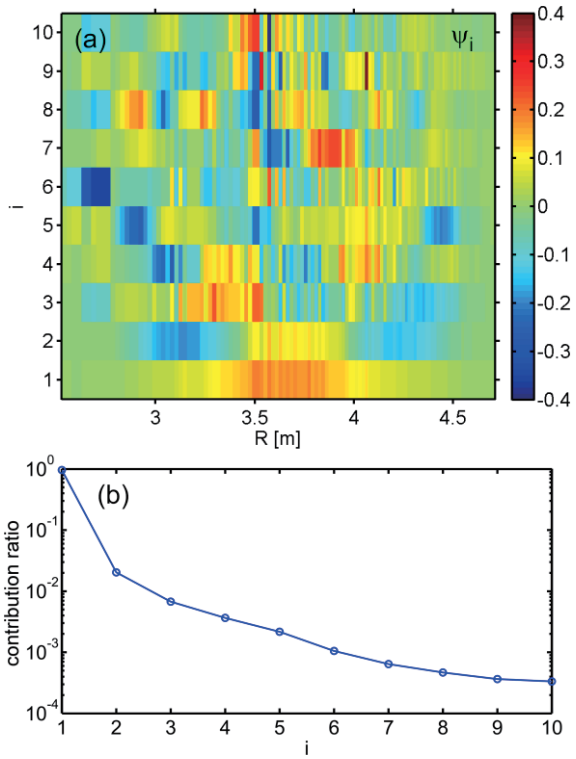

Fig. 3 (a) $\psi_i(R)$ as functions of R and mode number i from $i = 1$ to 10 and (b) its contribution ratio as a function of i.

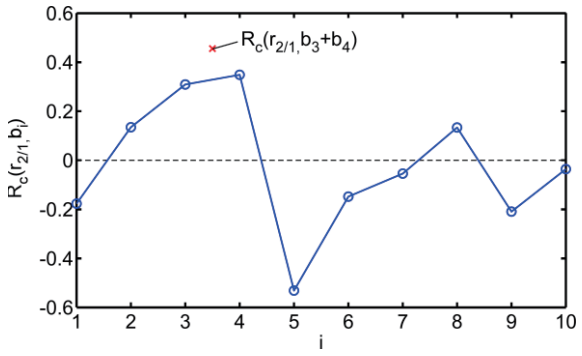

Fig. 4 $R_c(r_{2/1}, b_i)$ as a function of i (blue circle) and $R_c(r_{2/1}, b_3 + b_4)$ (red cross).

4.2 Relationship between divertor footprint index and POD modes of core plasma distribution

To clarify the relationship between the divertor footprint index and the obtained mode structures in the core plasma region, we calculated the cross-correlation coefficient between $r_{2/1}$ and b_i in dataset B by the following equation:

$$R_c(r_{2/1}, b_i) = \langle \tilde{r}_{2/1}(t)\tilde{b}_i(t)\rangle / \langle \tilde{r}_{2/1}^2\rangle^{0.5}\langle b_i^2\rangle^{0.5}. \quad (9)$$

Figure 4 shows $R_c(r_{2/1}, b_i)$ as a function of i. Positive correlation coefficients are seen for $i = 3$ and 4 modes with $R_c \sim 0.31$ and ~0.35, respectively. In contrast, a negative correlation is clearly observed for $i = 5$ mode with $R_c \sim -0.53$. Therefore, conditions that $b_3 > 0$, $b_4 > 0$, and $b_5 < 0$ contribute to an increase in $r_{2/1}$ at which a peak in particle flux appears at the SOL-side divertor probes. The other modes are not so correlated with the divertor footprint distribution. In the following, we focus on $i = 3$, 4, and 5 modes.

Figure 5 shows spatial distributions of ψ_3, ψ_4, and ψ_5. In this figure, edge regions inside the last closed flux surface (LCFS) with the normalized minor radius of $\rho \sim 0.85$ - 0.95 are hatched. ψ_3 and ψ_4 have similar shapes near the magnetic axis position, positive for $R < R_{ax}$ and negative for $R > R_{ax}$. In the more outer edge region, ψ_3 and ψ_4 are negative at outer and inner major radius positions, respectively. Because b_3 and b_4 are positively correlated with $r_{2/1}$, the similar feature around the magnetic axis could be important in changing the divertor footprint distribution. To simplify the interpretation, we assumed that the components of ψ_3 and ψ_4 affecting $r_{2/1}$ were attributed to the same mechanism. The cross-correlation between $r_{2/1}$ and the sum of two modes, $b_3 + b_4$, was calculated, as shown in Fig. 4. A larger positive correlation of $R_c(r_{2/1}, b_3 + b_4) \sim 0.46$ was confirmed.

On the other hand, ψ_5 has negative peaks at $\rho \sim 0.9$ as well as near the magnetic axis. In the previous study [9], it was reported that $r_{2/1}$ becomes small when the radial gradient of p_e at the peripheral region of $\rho \sim 0.9$ is steep. Therefore, observed negative peaks in the edge of ψ_5 could affect

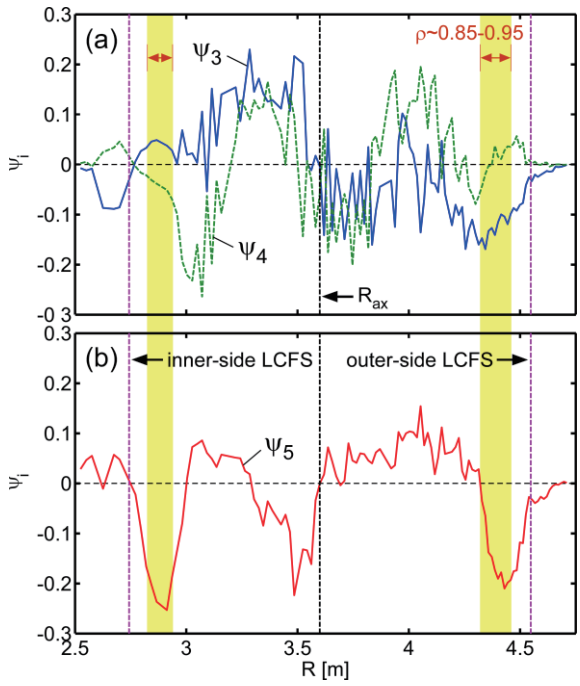

Fig. 5 (a) $\psi_3(R)$ (blue solid line), $\psi_4(R)$ (green dashed line), and (b) $\psi_5(R)$ (red solid line) as a function of R.

$r_{2/1}$. Detailed relationship between ψ_5 and p_e distributions will be discussed later.

Figure 6 (a) is a scatter plot with $b_3 + b_4$ on the horizontal axis, b_5 on the vertical axis, and $r_{2/1}$ as the color of the markers. Clearly, $r_{2/1}$ is smaller when $b_3 + b_4$ is smaller and b_5 is larger.

In order to discuss each impact independently, a limited range plot of another parameter was made. Figure 6 (b) shows $b_3 + b_4$ as a function of $r_{2/1}$ under the condition that $|b_5| < 1.0$, which corresponds to less than a half of the standard deviation of b_5. Positive correlation can be seen, as expected from the correlation analysis result, but there is a large variation and some point groups do not follow the fitted linear curve depicted by a dashed line. This means that $r_{2/1}$ is not strongly determined from $b_3 + b_4$ and there might be influences from other modes.

Similar to Fig. 6 (b), the $r_{2/1}$-dependence of b_5 under the condition that $|b_3 + b_4| < 2.3$ is shown in Fig. 6 (c). The variation of b_5 is large when $r_{2/1}$ is positive, and smaller when $r_{2/1}$ is negative. This result indicates that positive b_5 contributes more strongly to reduce $r_{2/1}$, i.e., to form the private-side peak on the divertor footprint (see Fig. 2).

4.3 Relationship to core plasma distribution and discussion

To understand the relationship between POD analysis results and the core plasma distribution, the p_e distributions at characteristic time points were extracted. Figure 7 shows p_e as a function of R at four time points, t_1, t_2, t_3, and t_4. In Fig. 6, markers at these time points are indicated by green circles. At the former two points, t_1 and t_2, $r_{2/1}$

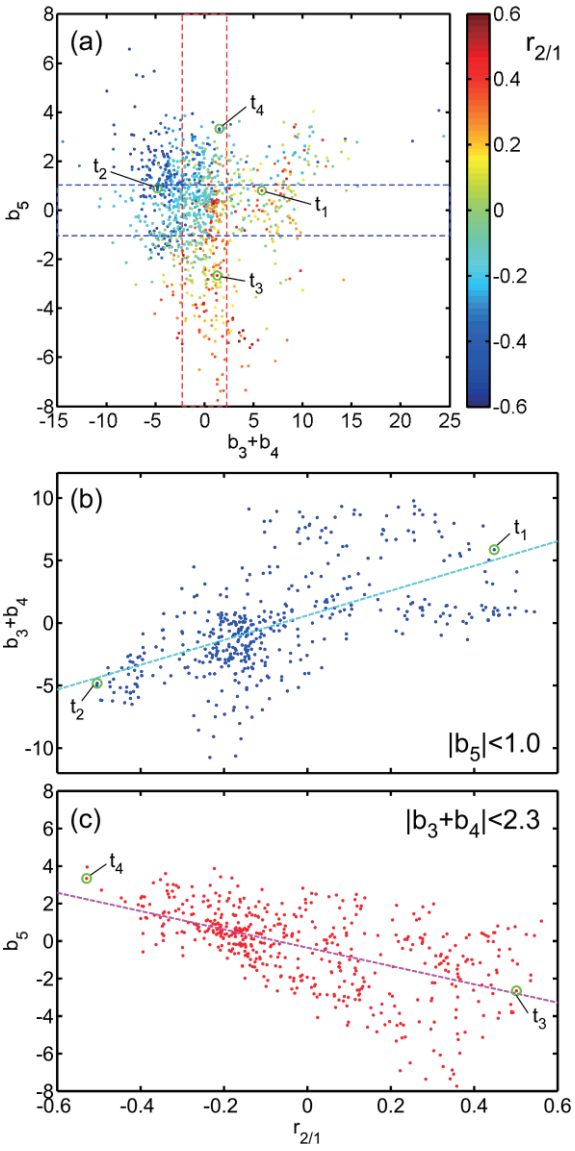

Fig. 6 (a) Scatter plot of b_5 versus $b_3 + b_4$. Dot color indicates $r_{2/1}$. (b) $b_3 + b_4$ and (c) b_5 as a function of $r_{2/1}$ under the conditions that $|b_5| < 1.0$ and $|b_3 + b_4| < 2.3$, respectively.

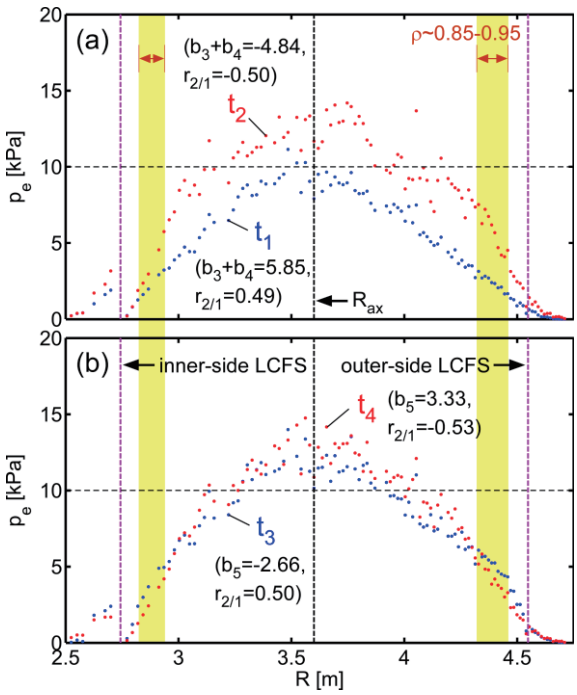

Fig. 7 p_e distributions at time points (a) t_1 (blue), t_2 (red), (b) t_3 (blue), and t_4 (red).

values are large and small, respectively, in Fig. 6 (b). Similarly, at the latter two time points, t_3 and t_4, $r_{2/1}$ values are large and small, respectively, in Fig. 6 (c).

At the time point t_1, the p_e distribution is relatively line symmetric about the magnetic axis. On the other hand, the p_e distribution at t_2 is somewhat larger and complicated. From Fig. 5 (a), when b_3 and b_4 are negative, $b_3\psi_3$ and $b_4\psi_4$ contribute to create a peak at $R \sim 3.75$ m, which is slightly outward from the magnetic axis position. In fact, the p_e distribution at t_2 seems to have a peak around there, although it is not distinct. The peak shift outward might be attributed to the Shafranov shift with relatively high plasma pressure (finite β), and such the condition is known to change the divertor footprint [6]. Therefore, the positive correlation between $b_3 + b_4$ and $r_{2/1}$ might be explained by the finite β effect. Note that the overall increase in p_e also increases the peripheral gradient, which may have an additional effect regarding the Pfirsch-Schlüter current discussed below.

Comparing p_e at time points t_3 and t_4 in Fig. 6 (b), we can see that these shapes are similar but the slope is steeper at $\rho \sim 0.9$ at t_4, in which b_5 is positive. This feature is consistent with the distribution of b_5, which has the convex shape on the negative side at $\rho \sim 0.9$ (see Fig. 5 (b)). The previous study reported that when the peripheral p_e has a steep gradient, a private side peak appears in the divertor particle flux distribution [9], which would be due to the modification of the edge magnetic field structure caused by the Pfirsch-Schlüter current [17, 18]. The Pfirsch-Schlüter current is a representative parallel current in helical devices and is driven by the plasma pressure gradient. The movement of magnetic field structure relative to the divertor plate changes the particle flux distribution on the divertor plate [9]. Therefore, the negative correlation between b_5 and $r_{2/1}$ can be attributed to the steep gradient of the p_e distribution and its modification effect on the edge magnetic field structure.

5. Summary

We have applied the multivariable analysis technique called the proper orthogonal decomposition (POD) to the electron pressure (p_e) distribution in the core region of LHD in addition to the divertor particle flux distribution which was previously analyzed. Furthermore, we investigated the relationship between the orthogonal modes of the core plasma distribution and the divertor footprint index

($r_{2/1}$) which characterizes whether the particle flux distribution peaks on the private or SOL side on the inner divertor plate.

The POD analysis gave dominant spatial orthogonal distributions (ψ_i) of p_e and their coefficients (b_i) at each time point. Cross-correlation analysis indicates that 3rd, 4th, and 5th modes are highly correlated with $r_{2/1}$. Moreover, the sum of 3rd and 4th mode coefficients, $b_3 + b_4$, shows stronger correlation with $r_{2/1}$. In order to independently examine the effects of $b_3 + b_4$ and b_5 on $r_{2/1}$, the dependence was studied by limiting the parameter range of one of them. As a result, although there was a finite variation, positive and negative correlations were clearly observed with $b_3 + b_4$ and b_5, respectively.

Both the ψ_3 and ψ_4 shapes seem to correspond to the shift of the p_e peak position from the magnetic axis position. In contrast, ψ_5 has a strong influence on the peripheral gradient of p_e. Therefore, the effect of the former bases on the divertor particle flux distribution might be related to the finite β effect, while the latter changing $r_{2/1}$ would be related to the Pfirsch-Schlüter current. It should be noted that the Pfirsch-Schlüter current effect is likely to be included in the former case, because the high plasma pressure with high β equips a high edge pressure gradient. In any case, these effects would alter the edge magnetic field structure outside the LCFS, which changes the divertor particle flux distribution. In contrast, ψ_2, which makes p_e distribution peaking/flattening around the radial center, does not have a strong correlation with $r_{2/1}$. This means that p_e peaking/flattening near the magnetic axis is not so related to the divertor particle flux distribution.

To verify these effects, it is effective to perform magnetic field calculations and 3D numerical simulations with EMC3-EIRENE code [19], which take the magnetic field modification effects into account, and compare calculation results with experiments. In addition, although this study focused on the analysis of divertor particle flux, divertor heat flux is of greater importance to engineering. Investigations on distributions of the heat flux measured with an infrared camera [20] and Langmuir probes are desirable in LHD. Also, to directly confirm the relationship between the Shafranov shift and related orthogonal bases, the correlation analysis with the magnetic axis position obtained by the best-fitted equilibrium is a future task.

In this study, the POD analysis can extract the main bases of the core plasma distribution strongly related to the divertor particle flux distribution. This method can be used to study the dependence on various parameters, except for phenomena that depend on time derivatives. To investigate such the phenomena with time-transient modes, the dynamic mode decomposition (DMD) [21–24] can be used.

Acknowledgements

The authors wish to thank the LHD experiment group for the excellent support of this work. This work was also supported by KAKENHI (18KK0410), NIFS Collaboration Research Program (NIFS22KIPP002), The Nitto Foundation, and NINS program of Promoting Research by Networking among Institutions (Grant Number 01411702).

Data Availability Statement

The LHD data can be accessed from the LHD data repository at https://www-lhd.nifs.ac.jp/pub/Repository_en.html.

[1] T. Eich *et al.*, Nucl. Fusion **53**, 093031 (2013).
[2] S. Masuzaki *et al.*, Nucl. Fusion **42**, 750 (2002).
[3] G.A. Wurden *et al.*, Nucl. Fusion **57**, 056036 (2017).
[4] F. Effenberg *et al.*, Nucl. Mater. Energy **18**, 262 (2019).
[5] S. Masuzaki *et al.*, Nucl. Fusion **53**, 112001 (2013).
[6] S. Masuzaki *et al.*, Fusion Sci. Technol. **50**, 361 (2006).
[7] S. Masuzaki *et al.*, Contrib. Plasma Phys. **50**, 629 (2010).
[8] S. Dai *et al.*, Plasma Phys. Control. Fusion **59**, 085013 (2017).
[9] H. Tanaka *et al.*, Plasma Phys. Control. Fusion **60**, 125001 (2018).
[10] H. Tanaka *et al.*, Nucl. Mater. Energy **19**, 378 (2019).
[11] M. Emoto *et al.*, Fusion Eng. Des. **81**, 2019 (2006).
[12] P. Holmes *et al.*, *Turbulence, Coherent Structures, Dynamical Systems and Symmetry* (Cambridge University, Cambridge, 1996) p. 86.
[13] H. Tanaka *et al.*, Contrib. Plasma Phys. **50**, 256 (2010).
[14] S. Ohdachi *et al.*, Plasma Sci. Technol. **8**, 45 (2006).
[15] Y. Asahi *et al.*, Phys. Plasmas **28**, 012304 (2021).
[16] K. Mukai *et al.*, Nucl. Mater. Energy **33**, 101294 (2022).
[17] Y. Suzuki *et al.*, Contrib. Plasma Phys. **50**, 576 (2010).
[18] Y. Suzuki *et al.*, 21st Int. Stellarator-Heliotron Workshop (ISHW2017) (Kyoto, Japan, 2-6 October) (2017).
[19] G. Kawamura *et al.*, Plasma Phys. Control. Fusion **60**, 084005 (2018).
[20] Y. Hayashi *et al.*, Fusion Eng. Des. **165**, 112235 (2021).
[21] P. Schmid, J. Fluid Mech. **656**, 5 (2010).
[22] C. Rowley *et al.*, J. Fluid Mech. **641**, 115 (2009).
[23] M. Sasaki *et al.*, Plasma Phys. Control. Fusion **61**, 112001 (2019).
[24] H. Natsume *et al.*, Phys. Plasmas **27**, 042301 (2020).